

Well-Balanced Finite Volume Scheme for Shallow Water Flooding and Drying Over Arbitrary Topography

Yuxin Huang, Ningchuan Zhang & Yuguo Pei

To cite this article: Yuxin Huang, Ningchuan Zhang & Yuguo Pei (2013) Well-Balanced Finite Volume Scheme for Shallow Water Flooding and Drying Over Arbitrary Topography, Engineering Applications of Computational Fluid Mechanics, 7:1, 40-54, DOI: [10.1080/19942060.2013.11015452](https://doi.org/10.1080/19942060.2013.11015452)

To link to this article: <https://doi.org/10.1080/19942060.2013.11015452>



Copyright 2013 Taylor and Francis Group LLC



Published online: 19 Nov 2014.



Submit your article to this journal [↗](#)



Article views: 1443



View related articles [↗](#)



Citing articles: 4 View citing articles [↗](#)

WELL-BALANCED FINITE VOLUME SCHEME FOR SHALLOW WATER FLOODING AND DRYING OVER ARBITRARY TOPOGRAPHY

Yuxin Huang *, Ningchuan Zhang and Yuguo Pei

State Key Laboratory of Coastal and Offshore Engineering, Dalian University of Technology, Dalian, 116024, China

** E-Mail: yxhuang1985@gmail.com (Corresponding Author)*

ABSTRACT: The depth-averaged shallow water equations based on Godunov-type finite volume method are developed for unsteady flow over arbitrary topography with moving lateral boundaries caused by flooding or recession. An HLLC approximate Riemann solver is invoked to evaluate fluxes. A linear reconstruction procedure with WBAP-L1 limiter and modified 4 stages Runge-Kutta time stepping are employed to provide a second order accuracy that is free from spurious oscillations. Also, a robust technique is presented to efficiently and accurately simulate the movement of wet/dry fronts. The model predictions are compared with analytical solutions, experimental data and a two-dimensional dam-break event. Numerical results show that the model performs satisfactorily with respect to its effectiveness and robustness and thus has good application prospects.

Keywords: shallow water flow, finite volume method, unstructured grid, HLLC scheme, wet/dry fronts, complex topography

1. INTRODUCTION

In the management of water resources, the shallow water flow model has been well established for describing numerous free surface flow problems. The applications can be found in a variety of areas of fluid dynamics, including the prediction of dam breaks, river and lake hydrodynamics, long wave run-up, as well as estuarine and coastal circulations.

A series of great improvements in numerical models of free surface flow have been achieved in the last decade. Various computational techniques have been proposed to discretize the shallow water equations (hereafter referred to as SWEs), of which the three commonly used methods are finite difference method (FDM) (Glaister, 1988; Younus, 1994), finite element method (FEM) (Navon, 1979; Heniche et al., 2000; Hanert et al., 2005) and finite volume method (FVM) (Bermudez and Vázquez, 1994; Zhao et al., 1994; Vázquez, 1999; Garcia-Navarro and Vázquez, 2000; Zhou et al., 2001; Valiani et al., 2002; Brufau et al., 2004; Begnudeli and Sanders, 2004; Liang and Borthwick, 2009; Song et al., 2010). The superiority of FVM for high speed flows has been demonstrated by model tests. The main advantages are: the local and global mass conservation property, the flexibility in applying for irregular domains by unstructured grids, and reduction in the burden of explicit calculation

memory requirement (Loukili and Soulaïmani, 2007).

Godunov-type finite volume schemes (Toro, 2001; LeVeque, 2002) are based on discretization of the computational domain into subdomains over where the equations are integrated and evolving the solution forward in time. Shock capturing capabilities are provided by solving a series of one dimensional (1D) Riemann problems for fluxes on the interface between neighboring cells. In the well-known work of Godunov (1959), the exact solution of the Riemann problem was performed. In order to reduce computational time, the exact solution of the Riemann problem is nowadays replaced by an approximate approach, which is referred to as Flux Difference Splitting (FDS). Several researchers have been contributing in the field of approximate Riemann solvers in the last three decades. Remarkable results that obtained in aerodynamics have increasingly been extended to solve the shallow water system. There are, for example, Roe's scheme (Roe, 1981), flux-vector splitting (FVS) scheme (Steger and Warming, 1981), Osher scheme (Osher and Solomon, 1982), HLL scheme (Harten, et al., 1983), and HLLC scheme (Toro et al., 1994), which have also largely been evaluated through idealized benchmark test cases and field-scale shallow flow modeling applications (Bermudez and Vázquez, 1994; Toro, 2001; Brufau et al., 2004; Zhou et al., 2004; Loukili, 2007; Liang, 2009; Song et al., 2011).

The imbalance problem is particularly acute for the SWEs with the presence of source terms in describing a realistic geometry. This issue is addressed by several authors. Bermudez and Vázquez (1994) proposed an upwind treatment of the source terms in the Roe-type finite volume scheme. The approach is then extended and validated to consider a wider range of flow problems (Bermudez et al., 1998; Vázquez, 1999; Garcia-Navarro and Vázquez 2000). The trouble of water at rest on an uneven bed has been tackled, among others, by Nujic (1995). LeVeque (1998) introduced a quasi-steady wave-propagation algorithm by artificially invoking another discontinuity within each computational cell to account for the propagation of source terms, while Mohanraj et al. (1999) used a characteristics based treatment of the source terms. Zhou et al. (2001) introduced the surface gradient method and argued that interpolating the depth without considering the bed variations may lead to erroneous results. Rogers et al. (2003) proposed an alternative method that uses surface elevation and still water depth to replace the total water depth to split the free surface gradient term.

Flow over dry bed involves a complicated boundary condition which is dynamically changing in time with the moving front and continuously expanding or reducing the flow domain. In FVM where the depth-averaged velocity components are normally determined by dividing the discharge per unit width by the local water depth, unphysical high velocities can be predicted at wet/dry fronts where the water depth is extremely small. These can lead in turn to predictions of negative water depth and numerical instability. Although a variety of wetting and drying algorithms have been proposed, especially for the hyperbolic SWEs (e.g. Zhao et al., 1994; Fraccarollo and Toro, 1995; Sleight et al., 1998; Brufau et al., 2004; Zhou et al., 2004; Begnudelli and Sanders, 2006; Liang and Borthwick, 2009; Song et al., 2011), most of these methods are not applicable and further research is required.

The present works concentrate on developing and testing the unstructured grid Godunov-type FVM based 2D shallow water model, which can simulate unsteady flow over arbitrary topography. An HLLC approximate Riemann solver, together with the linear reconstruction procedure, is employed to evaluate the normal fluxes across the cell faces. For the scheme of the modified 4 stages Runge-Kutta method used in time stepping, the proposed scheme provides a second order convergent accuracy in both spatial and temporal discretization. Furthermore, based on the existing

method (Zhao et al., 1994) this model utilizes an improved approach to efficiently predict the wetting and drying fronts, where a flux correction strategy is added to ensure mass conservation. The performance of the new model is further validated by several numerical tests. The numerical results show that the present model performs satisfactorily and thus has good application prospects.

2. NUMERICAL METHOD

The 2D non-linear SWEs can be derived by integrating the 3D Reynolds-averaged Navier-Stokes equations over the depth, neglecting the vertical acceleration of water particles, and taking the pressure distribution to be hydrostatic (Toro, 2001). The conserved type 2D SWEs can be expressed as

$$\frac{\partial \mathbf{U}}{\partial t} + \nabla(\mathbf{G}, \mathbf{H}) = \mathbf{S} + \nabla(\mathbf{G}^d, \mathbf{H}^d), \text{ in } A \times [0, T_s] \quad (1)$$

in which

$$\begin{aligned} \mathbf{U} &= (\eta, uh, vh)^T, \\ \mathbf{G} &= (uh, hu^2, uvh)^T, \\ \mathbf{H} &= (vh, uvh, hv^2)^T, \\ \mathbf{S} &= (0, \tau_{sx}/\rho - ghS_{bx} - gh\partial\eta_x/hf, \\ &\quad \tau_{sy}/\rho - ghS_{by} - gh\partial\eta_y/hf)^T \end{aligned} \quad (2)$$

and

$$\begin{aligned} \mathbf{H}^d &= (0, vh(\partial u_y + \partial v_x), vh(2\partial v_y))^T, \\ \mathbf{G}^d &= (0, vh(2\partial u_x), vh(\partial u_y + \partial v_x))^T, \end{aligned} \quad (3)$$

where

A: domain representing the horizontal cross-section of water body.

T_s : total simulation time.

η : water elevation above still water level.

h : total water depth ($= \eta - z_b$) (Fig. 1).

u, v : depth-averaged velocity components in the x - and y - direction, respectively.

g : acceleration due to gravity.

f : Coriolis force parameter.

ρ : water density.

ν : horizontal eddy viscosity (m^2s^{-1}).

τ_{sx}, τ_{sy} : surface stresses in the x - and y - direction, respectively.

S_{bx}, S_{by} : bed friction terms in the x - and y - direction, respectively.

$$S_{bx} = \frac{n^2 u \sqrt{u^2 + v^2}}{h^{4/3}}, \quad S_{by} = \frac{n^2 v \sqrt{u^2 + v^2}}{h^{4/3}} \quad (4)$$

n : Manning's roughness coefficient.

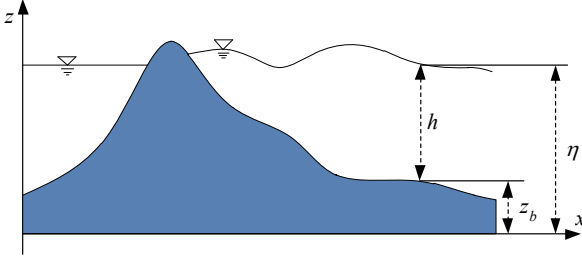


Fig. 1 Schematic diagram of unsteady flow over irregular bottom.

In order to facilitate the solving procedure with a Godunov-type scheme, it is necessary to rewrite Eqs. (1) - (3) as a system of hyperbolic equations. To achieve this, it is conventional to split the $gh\partial\eta_x$ and $gh\partial\eta_y$ terms in Eq. (2) between flux gradients and source terms (e.g. Zhao, 1994). Taking the x -direction momentum equation as an instance

$$gh \frac{\partial \eta}{\partial x} = \frac{1}{2} g \frac{\partial h^2}{\partial x} + ghS_{ox} \quad (5)$$

where $S_{ox} = \partial z_b / \partial x$ is the bed slope term in x -direction. A similar treatment is applied in the y -direction. Therefore, the following hyperbolic matrix system of conservation laws for the SWEs can be derived:

$$\begin{aligned} \mathbf{U} &= (\eta, uh, vh)^T, \\ \mathbf{G} &= (uh, hu^2 + gh^2/2, uvh)^T, \\ \mathbf{H} &= (vh, uvh, hv^2 + gh^2/2)^T, \\ \mathbf{S} &= (0, \tau_{sx}/\rho - ghS_{bx} - g\eta S_{ox} + hfv, \\ &\quad \tau_{sy}/\rho - ghS_{by} - g\eta S_{oy} - hf u)^T. \end{aligned} \quad (6)$$

However, Rogers et al. (2003) had proved that this type of SWEs cannot be directly used when the bed topography is non-uniform. Rogers et al. (2003) presented a different way to splitting the surface gradient term to ensure that flux gradient and bed slope source terms are balanced mathematically, then Liang and Borthwick (2009) improved this method for treatment of wetting/drying process.

$$gh \frac{\partial \eta}{\partial x} = \frac{1}{2} g \frac{\partial (\eta^2 - 2\eta z_b)}{\partial x} + ghS_{ox} \quad (7)$$

Same procedure for y -direction, the vector terms for the shallow water equations now become

$$\begin{aligned} \mathbf{U} &= (\eta, uh, vh)^T, \\ \mathbf{G} &= (uh, hu^2 + g(\eta^2 - 2\eta z_b)/2, uvh)^T, \\ \mathbf{H} &= (vh, uvh, hv^2 + g(\eta^2 - 2\eta z_b)/2)^T, \\ \mathbf{S} &= (0, \tau_{sx}/\rho - ghS_{bx} - g\eta S_{ox} + hfv, \\ &\quad \tau_{sy}/\rho - ghS_{by} - g\eta S_{oy} - hf u)^T. \end{aligned} \quad (8)$$

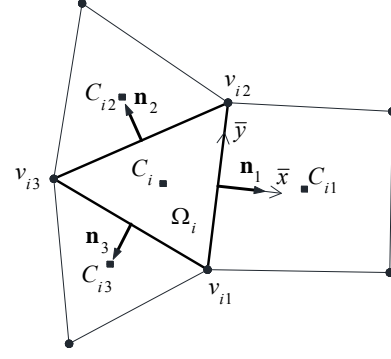


Fig. 2 Control volume of cell-centered scheme.

Eqs. (1), (3) and (8) are the final type of 2D unsteady SWEs adopted in this paper.

2.1 Finite volume method

In this study, a cell-centered Godunov-type FVM is adopted to solve the SWEs. The computational domain is divided into a set of triangular or quadrilateral grids (Fig. 2). Then Eq. (1) is integrated over each control volume by application of the Green's theorem, which yields

$$\frac{\partial}{\partial t} \int_{\Omega} \mathbf{U} d\Omega + \oint_{\partial\Omega} \mathbf{F} \cdot \mathbf{n} dl = \int_{\Omega} \mathbf{S} d\Omega + \oint_{\partial\Omega} \mathbf{F}^d \cdot \mathbf{n} dl \quad (9)$$

in which Ω denotes the control volume, $\partial\Omega$ the boundary of the volume, \mathbf{n} the unit outward vector normal to the boundary, and $d\Omega$ and dl are the area and arc elements, respectively. The integrand $\mathbf{F} \cdot \mathbf{n}$ and $\mathbf{F}^d \cdot \mathbf{n}$ are the convective and diffusive outward normal flux vectors, in which $\mathbf{F} = [\mathbf{G}, \mathbf{H}]^T$ and $\mathbf{F}^d = [\mathbf{G}^d, \mathbf{H}^d]^T$.

After discretizing, Eq. (9) becomes

$$\begin{aligned} \frac{\mathbf{U}^{n+1} - \mathbf{U}^n}{\Delta t} &= -\frac{1}{\Omega} \sum_{j=1}^m \mathbf{F}_j(\mathbf{U}_L, \mathbf{U}_R) \cdot \mathbf{n}_j l_j \\ &+ \frac{1}{\Omega} \sum_{k=1}^m \mathbf{F}_j^d(\mathbf{U}_L, \mathbf{U}_R) \cdot \mathbf{n}_j l_j + \mathbf{S} \end{aligned} \quad (10)$$

where m represents the number of cell sides, l_j the length of side j , and $\mathbf{n}_j = (n_x, n_y)^T$ the restriction of \mathbf{n} to the face j . Consider the rotation matrix and its inverse matrix

$$\mathbf{T}_n = \begin{bmatrix} 1 & 0 & 0 \\ 0 & n_x & n_y \\ 0 & -n_y & n_x \end{bmatrix}, \quad \mathbf{T}_n^{-1} = \begin{bmatrix} 1 & 0 & 0 \\ 0 & n_x & -n_y \\ 0 & n_y & n_x \end{bmatrix} \quad (11)$$

By using the rotational invariance property of the SWEs (LeVeque, 2002), we have

$$\mathbf{F}_j(\mathbf{U}_L, \mathbf{U}_R) \cdot \mathbf{n}_j = \mathbf{T}_{n,j}^{-1} \mathbf{G}(\mathbf{T}_{n,j} \mathbf{U}_L, \mathbf{T}_{n,j} \mathbf{U}_R) \quad (12)$$

Let

$$\hat{\mathbf{U}} = \mathbf{T}_n \mathbf{U} = (\eta, hu^\perp, hu^\parallel)^T \quad (13)$$

where $u^\perp = un_x + vn_y$ and $u^\parallel = vn_x - un_y$ are the velocity perpendicular and tangential to the cell face, respectively. Then

$$\mathbf{F}(\mathbf{U}) \cdot \mathbf{n} = \mathbf{T}_n^{-1} \mathbf{G}(\hat{\mathbf{U}}) = \begin{bmatrix} \eta u^\perp \\ h u u^\perp + g(\eta^2 - 2\eta z_b) n_x / 2 \\ h v u^\perp + g(\eta^2 - 2\eta z_b) n_y / 2 \end{bmatrix} \quad (14)$$

The diffusive fluxes \mathbf{F}^d on the cell interfaces are usually approximated by a centered scheme

$$\mathbf{F}^d = (\mathbf{F}_L^d + \mathbf{F}_R^d) / 2 \quad (15)$$

and the convective fluxes \mathbf{F} are calculated by HLLC approximate Riemann solver.

2.2 HLLC approximate Riemann solver

HLLC scheme is a modified version of the HLL scheme (Harten et al., 1983), which was first introduced by Toro et al. (1994) for solving the Euler equations. Unlike HLL, HLLC considers the middle characteristic. The Riemann structure has the form shown in Fig. 3. According to literature (Toro, 2001), the interface fluxes $\mathbf{F}(\mathbf{U}) \cdot \mathbf{n}$ are evaluated by

$$\mathbf{F}(\mathbf{U}_L, \mathbf{U}_R) \cdot \mathbf{n} = \begin{cases} \mathbf{F}_L & \text{if } s_L \geq 0 \\ \mathbf{F}_{*L} & \text{if } s_L < 0 \leq s_* \\ \mathbf{F}_{*R} & \text{if } s_* < 0 \leq s_R \\ \mathbf{F}_R & \text{if } s_R \leq 0 \end{cases} \quad (16)$$

where $\mathbf{F}_L = \mathbf{F}(\mathbf{U}_L) \cdot \mathbf{n}$ and $\mathbf{F}_R = \mathbf{F}(\mathbf{U}_R) \cdot \mathbf{n}$ with \mathbf{U}_L and \mathbf{U}_R represent the left and right Riemann states of a local Riemann problem, respectively; \mathbf{F}_{*L} and \mathbf{F}_{*R} are the numerical fluxes in the left and right parts of the middle region of the Riemann solution which is divided by a contact (shear) wave; and s_L , s_* and s_R are the speeds of the left, contact and right waves. If subscripts 1 and 2 are used to denote the first and second components, respectively, the flux vectors \mathbf{F} , \mathbf{F}_{*L} and \mathbf{F}_{*R} can be expressed as

$$\mathbf{F}_{*L} = (F_{1*}, F_{2*}, F_{1*} u_L^\parallel)^T, \quad \mathbf{F}_{*R} = (F_{1*}, F_{2*}, F_{1*} u_R^\parallel)^T \quad (17)$$

where u_L^\parallel and u_R^\parallel are the left and right tangential velocity components of the local Riemann states, respectively; and F_{1*} and F_{2*} in the middle region are calculate from the HLL formula given by Harten et al. (1983),

$$\mathbf{F}_* = \frac{s_R \mathbf{F}_L - s_L \mathbf{F}_R + s_L s_R (\hat{\mathbf{U}}_R - \hat{\mathbf{U}}_L)}{s_R - s_L} \quad (18)$$

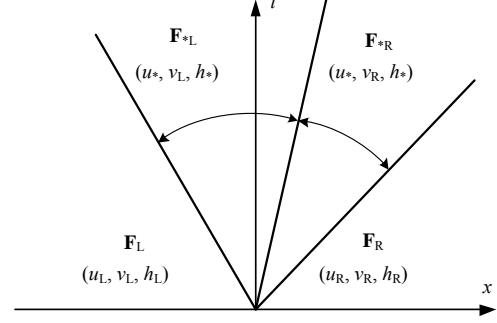


Fig. 3 HLLC solution structure of Riemann problem.

Wave speeds s_L , s_* and s_R have significant effect on the numerical fluxes, then an appropriate method for wave speeds approximation is the key to the success of HLLC solver. Fraccarollo and Toro (1995) suggested the following approximations including dry-bed options from the two-rarefaction approximate Riemann solver, where the left and right wave speeds are determined from

$$s_L = \begin{cases} u_R^\perp - 2\sqrt{gh_R} & h_L = 0 \\ \min(u_L^\perp - \sqrt{gh_L}, u_* - \sqrt{gh_*}) & h_L > 0 \end{cases} \quad (19a)$$

and

$$s_R = \begin{cases} u_L^\perp + 2\sqrt{gh_L} & h_R = 0 \\ \max(u_R^\perp + \sqrt{gh_R}, u_* + \sqrt{gh_*}) & h_R > 0 \end{cases} \quad (19b)$$

where u_L^\perp , u_R^\perp , h_L and h_R are the left and right initial values for a local Riemann problem, calculated from

$$u_* = (u_L^\perp + u_R^\perp) / 2 + (c_L - c_R) \quad (20a)$$

and

$$h_* = [(\sqrt{gh_L} + \sqrt{gh_R}) / 2 + (u_L^\perp - u_R^\perp) / 4]^2 / g \quad (20b)$$

As to the middle wave speed, Toro (2001) demonstrated that the following choice is suitable for dry-bed problems:

$$s_* = \frac{s_L h_R (u_R^\perp - s_R) - s_R h_L (u_L^\perp - s_L)}{h_R (u_R^\perp - s_R) - h_L (u_L^\perp - s_L)} \quad (21)$$

2.3 Treatment of source terms

The irregularity of the topography plays an important role in real engineering applications and often has great impacts on the final accuracy of the results. Treating the friction source term with a simple explicit discretization may cause numerical instabilities if the water depth is small. Such situations may occur in particular at the

drying-wetting interfaces. To deal with this problem, a semi-implicit scheme is adopted to combine with splitting method for stability and computational efficiency (Song et al., 2010). Therefore the friction source term is calculated with the unknown value \mathbf{U}^{n+1} at the new time level as

$$\mathbf{U}^{n+1} = \mathbf{U}^{n+1/2} - \Delta t \mathbf{S}_b(\mathbf{U}^{n+1}) \quad (22)$$

Let $\tau = gn^2 h^{-4/3} \sqrt{(u^{n+1/2})^2 + (v^{n+1/2})^2}$ and implementing implicit scheme to Eq. (22), we have

$$\mathbf{U}^{n+1} = \left(\eta^{n+1/2}, \frac{(hu)^{n+1/2}}{1 + \Delta t \tau}, \frac{(hv)^{n+1/2}}{1 + \Delta t \tau} \right)^T \quad (23)$$

This scheme does not constrain the direction of velocity, i.e. $u^{n+1} \cdot u^{n+1/2} \geq 0$, and $v^{n+1} \cdot v^{n+1/2} \geq 0$, thus enhances the model stability.

If the cell Ω is triangular, the evaluation of the bed slope term is trivial, as the three vertices of the cell necessarily belong to a plane, and therefore S_{ox} and S_{oy} can be directly calculated by Green-Gauss theorem. For cells that have 4 vertices (Fig. 4), the evaluation of the terms S_{ox} and S_{oy} are not straightforward (and not unique, since it depends on the assumptions made regarding the bottom topography inside each cell). In this case, the technique proposed by Caleffi et al. (2003) has been chosen here to circumvent the problem. The bed elevation z_C of geometric centroid (x_C, y_C) is estimated by a weighted distance mean

$$z_C = \frac{\sum_{j=1}^4 z_j \sqrt{(x_j - x_C)^2 + (y_j - y_C)^2}}{\sum_{j=1}^4 \sqrt{(x_j - x_C)^2 + (y_j - y_C)^2}} \quad (24)$$

where $(z_j)_j = 1:4$ are the vertices' elevations. The local bottom slope for the quadrilateral is then evaluated as follows

$$S_{o\phi} = \sum_{j=1}^4 S_{o\phi,j} |K|_j / \sum_{j=1}^4 |K|_j, \quad \phi = x, y \quad (25)$$

where $S_{o\phi,j}$ is the slope of triangle $|K|_j$, obtained via the equation of the plane.

The surface stress and Coriolis source terms are directly communicated to in the cell by input file.

2.4 Boundary conditions

The numerical treatment of the boundary conditions is performed by setting the variables at the boundary edges based on the theory of

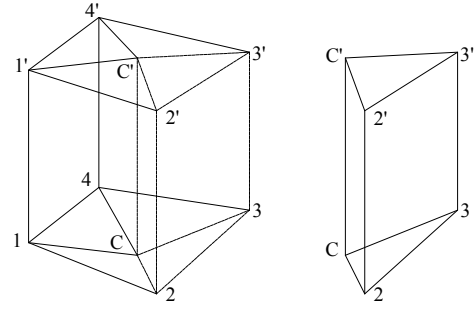


Fig. 4 Quadrangular cell and its division into four triangles.

characteristics (Alcrudo and Garcia-Navarro, 1993). For subcritical flows, two external conditions must be specified at inflow boundaries, whereas only one is required at the outflow boundaries. However, 2D supercritical flows require the imposition of three inflow boundary conditions and none at the downstream side. In the case of solid wall, normal velocity is set to zero. The depth variables are simply set to the corresponding values of the adjacent inner cells.

3. WET/DRY BOUNDARY TRACKING

For rivers and tidal zones, their boundaries change with time and varying water level. An important step of this model is to determine the water edge or the instantaneous computational boundary. In this study, wetting and drying technology developed by Zhao et al. (1994) has been refined and employed. To achieve the purpose of zero mass error, the method of Brufau et al. (2004) is also adopted here.

A criterion, ε , is used to classify the following three types of edges:

1. dry edge, when $h_L \leq \varepsilon$ and $h_R \leq \varepsilon$, as shown in Fig. 5a;
2. wet edge, when $h_L > \varepsilon$ and $h_R > \varepsilon$, as shown in Fig. 5b;
3. partially wet edge (no flux), left wet and right dry, for example, $h_L > \varepsilon$, $h_R \leq \varepsilon$ and $\eta_L \leq \eta_R$. For this case solid b.c. can be applied here, as shown in Fig. 5c;
4. partially wet edge (with flux), left wet and right dry for example, $h_L > \varepsilon$, $h_R \leq \varepsilon$ and $\eta_L > \eta_R$. The flow continues to flood the dry cell, as shown in Fig. 5d.

As to these four types of edges, cells will be correspondingly divided into three types:

1. wet cell, all the edges of this cell consists of wet edge or partially wet edge (with flux) and all the nodes of the cell must be flooded;

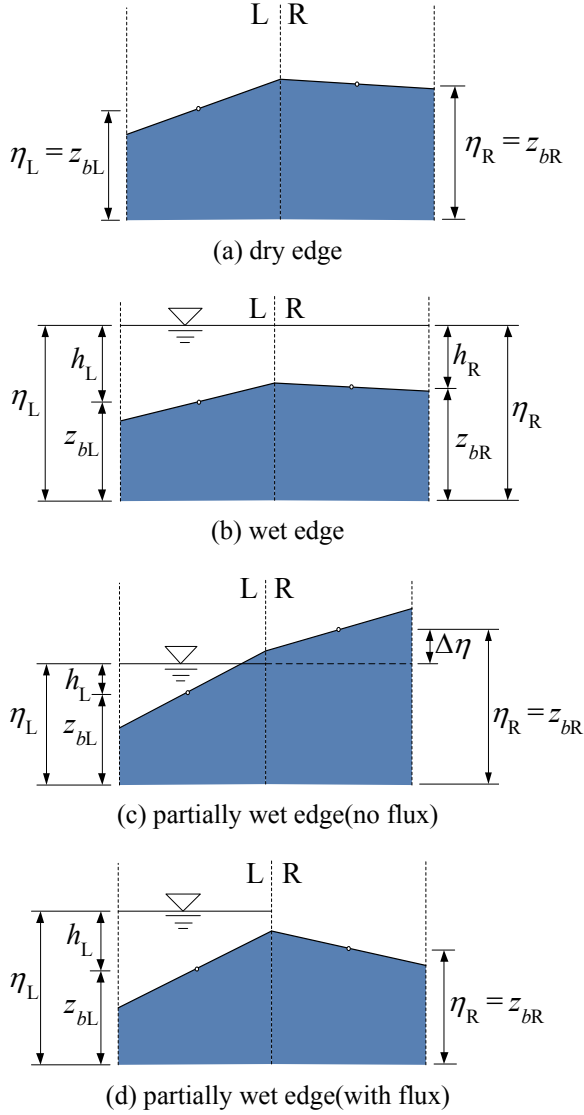


Fig. 5 Schematic diagram of wet-dry fronts.

2. dry cell, all the edges of this cell consists of dry edge or partially wet edge (no flux);
3. partially wet cell, in addition to all of the above.

If a cell is a partially wet cell, only mass flux will be taken into account and the momentum flux will be set to zero. When an edge is partially wet edge (no flux), there will be no flux across the interface wall. Without any modification however, the fact that $\eta_L \neq \eta_R$ will introduce a non-physical flux across the common cell interface. To overcome this problem, Liang and Borthwick (2009) presented a method that η_R and bed level z_{bR} for the dry cell temporarily are replaced by the following values of η'_R and z'_{bR} whenever the case in Fig. 5c is encountered

$$\eta'_R = \eta_R - \Delta\eta \text{ and } z'_{bR} = \eta'_R \quad (26)$$

With the solution advances, the continuity and momentum equations are updated in each cell. There may be situations in which more water is removed from an element than that is actually stored. As a result, the scheme becomes unstable. Such overdraft is mostly experienced in cases with strongly varying topography and low water depths. To prevent this kind of instability, the depth and velocity components are set to zero in any cell that has dried out. Then, the surrounding cells are checked and the same volume of water is subtracted from the neighbor cells to preserve mass conservation (Brufau et al., 2004).

4. MODELS' SECOND ORDER ACCURACY

4.1 Second order accuracy in space

In order to achieve second order accuracy in space, the cell boundary values are used instead of cell center ones. The variables are extrapolated to the boundaries by a linear reconstruction procedure

$$\mathbf{U}_i(\mathbf{r}) = \mathbf{U}_i + \nabla \mathbf{U}_i \cdot \mathbf{r} \quad (27)$$

where $\nabla \mathbf{U}_i$ represents the gradient of variable at the cell center and \mathbf{r} is the vector extending from the cell center to the midpoint of each edge, which are evaluated by a least-squares method proposed by Anderson and Bonhaus (1994).

According to Godunov's theorem, spurious oscillations in the vicinity of high gradients are expected (Toro, 1997), which is highly undesirable in any numerical scheme. The limiting procedures on unstructured grids are introduced to solve this problem. Among many others, the limiter of Barth and Jespersen (1989) is widely used. Li et al. (2011) presented that the Barth limiter is grid sensitive and more diffusive than WBAP limiter in 2D grids, while WBAP limiter is an improved type of BAP (Choi and Liu, 1998) limiter due to a weighted biased averaging procedure with the attractive properties of simple, efficient, parameter free, differentiable and applicable on unstructured grids. Here, a WBAP-L1 limiter was applied to the linear reconstruction procedure.

Let $S_i = \{C_{i1}, C_{i2}, C_{i3}\}$ (Fig. 2), then

$$\nabla \tilde{\mathbf{U}}_i = L(\nabla \mathbf{U}_i, \nabla \mathbf{U}_j, \dots), j \in S_i \quad (28)$$

$$L(a_0, a_1, a_2, \dots, a_j) = a_0 W(\theta_0, \theta_1, \theta_2, \dots, \theta_j), \theta_j = a_j / a_0 \quad (29)$$

$$W(\theta_0, \theta_1, \theta_2, \dots, \theta_J) = \begin{cases} \sqrt{\frac{n+J}{n + \sum_{j=1}^J 1/\theta_j^2}}, & \theta_1, \theta_2, \dots, \theta_J > 0 \\ 0, & \text{otherwise} \end{cases} \quad (30)$$

where n is the weight level of middle cell i , the recommended value $n = 5$ is adopted. Finally, the procedure becomes

$$\mathbf{U}_i(\mathbf{r}) = \mathbf{U}_i + \nabla \tilde{\mathbf{U}}_i \cdot \mathbf{r} \quad (31)$$

4.2 Second order accuracy in time

A second-order modified 4 stages Runge-Kutta (Dick, 2009) time stepping numerical solver, which has wide stability region, is employed on temporal items of the SWEs.

$$\begin{aligned} \mathbf{U}_i^0 &= \mathbf{U}_i^n \\ \mathbf{U}_i^k &= \mathbf{U}_i^0 + \alpha_k \Delta t L_i(\mathbf{U}^{k-1}), \quad k = 1, 2, 3, 4 \\ \mathbf{U}_i^{n+1} &= \mathbf{U}_i^4 \end{aligned} \quad (32)$$

with $\alpha_1=1/4$, $\alpha_2=1/3$, $\alpha_3=1/2$ and $\alpha_4=1$.

Due to the 4 stages Runge-Kutta is an explicit scheme, the time step Δt is need to be restricted by a Courant-Friendrichs-Lewy (CFL) condition

$$\text{CFL} = \Delta t \frac{2 \max_j (\sqrt{u^2 + v^2} + \sqrt{gh})_{ij}}{R_i} \quad (33)$$

where i represents the cell in computational domain, j is the surrounding cells of i , R_i is the distance between cell center to cell edge. CFL = 0.9 is adopted throughout the computational domains in this study.

5. NUMERICAL RESULTS AND DISCUSSION

Based on the above numerical scheme, a numerical model for solving SWEs has been developed by using the FORTRAN programming language. This model is verified by simulating two well established benchmark test cases in an ideal channel. Since the analytical solutions exist for these cases, the model's accuracy in dealing with various complicated flow situations can be guaranteed. Then, the case of complex dam-break flooding over three humps is carried out to evaluate the performance of the model in problems involving wetting-drying and mass conservation. The verified model is further validated by simulating a tsunami run-up flow in an experimental flume. Finally, the applicability in a realistic scenario is examined by simulating

the case of the Malpasset dam-break event which occurred in 1959 in France.

5.1 Still water at rest

Firstly, C-property (Bermudez and Vázquez, 1994) of our schemes should be tested. The case, still water steady state problem with a non-flat bottom and wet/dry interfaces, introduced by Brufau and Garcia-Navarro (2003) has been performed herein. The numerical experiment consists of a closed square pool of 1 m × 1 m. At the center of the pool a symmetric hump is situated, mathematically defined by

$$z_b(x, y) = \max[0, 0.25 - 4.8((x - 0.5)^2 + (y - 0.5)^2)] \quad (34)$$

There is no friction on the bottom and initial conditions are going to be analyzed with initial water level and the geography (as shown in Fig. 6)

$$\eta = 0.2 \text{ m}, u = 0 \text{ m/s and } v = 0 \text{ m/s} \quad (35)$$

In practical application, the equilibrium of still water should be exactly preserved with the initial conditions. We compute the solution until $t = 60$ s using five types of triangular meshes. In order to demonstrate the still water solution being indeed maintained up to round-off error, we use single- (SP) and double-precision (DP) to perform the computation. The resulting L^2 error norms for the surface elevation η and discharges of hu , hv are shown in Table 1. Well-balanced property, obviously, is verified by the round-off error for different number of cells and precisions.

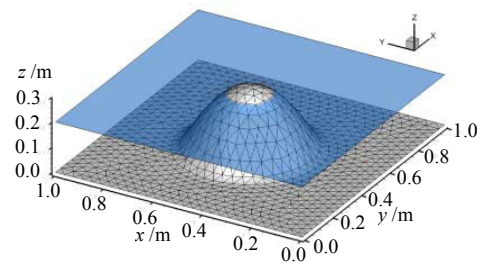


Fig. 6 3D plot of bottom topography for 2D hump (1670 triangular cells).

Table 1 L^2 error norms of still water test.

No. of cells	SP			DP		
	$L^2(\eta)$	$L^2(hu)$	$L^2(hv)$	$L^2(\eta)$	$L^2(hu)$	$L^2(hv)$
538	0	3.76E-06	3.90E-06	0	7.29E-15	7.16E-15
854	0	5.63E-06	5.53E-06	0	1.07E-14	1.01E-14
1210	0	5.91E-06	5.92E-06	0	1.12E-14	1.11E-14
1484	0	6.20E-06	6.21E-06	0	1.29E-14	1.28E-14
1670	0	6.45E-06	6.70E-06	0	1.30E-14	1.25E-14

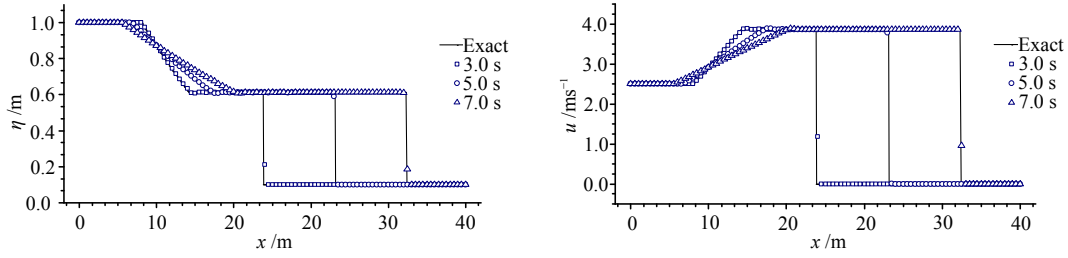


Fig. 7 Left critical rarefaction and right shock test case 1: depth(left) and velocity(right).

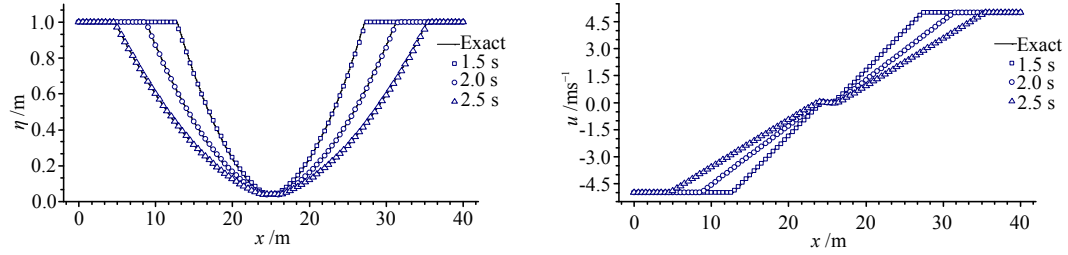


Fig. 8 Two rarefactions and nearly dry bed test case 2: depth(left) and velocity(right).

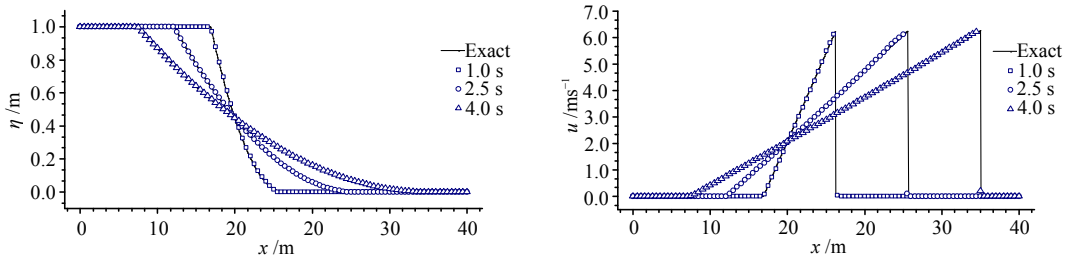


Fig. 9 Dam-break on dry bed test case 3: depth(left) and velocity(right).

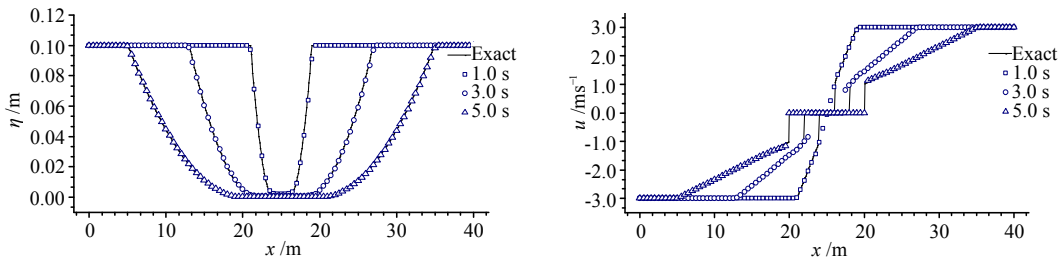


Fig. 10 Two rarefaction and dry middle state test case 4: depth(left) and velocity(right).

Table 2 Data for Toro's test problems.

Test	x_0 (m)	h_L (m)	u_L (m/s)	h_R (m)	u_R (m/s)	t_{out} (s)
1	10.0	1.0	2.5	0.1	0.0	7.0
2	25.0	1.0	-5.0	1.0	5.0	2.5
3	20.0	1.0	0.0	0.0	0.0	4.0
4	25.0	0.1	-3.0	0.1	3.0	5.0

Table 3 L^2 error norms of Toro's test (SP).

Test	$L^2(\eta)$	$L^2(hu)$
3.2.1	2.95E-04	2.53E-04
3.2.2	7.53E-04	4.58E-03
3.2.3	4.02E-04	6.79E-04
3.2.4	9.82E-05	3.13E-04

5.2 Toro's Riemann problems

We now investigate the performances of the proposed scheme with 1D Riemann tests using 2D model. The numerical solutions are compared with the analytical solutions provided by Toro (2001). A summary of initial conditions used in the tests are presented in Table 2, where h_L , u_L , h_R and u_R denote the initial depth and velocity in the left and right hand side of the discontinuity, respectively; x_0 is the position of the discontinuity and t_{out} is the output time. The computational parameters used during the simulations are adopted as follows, $\varepsilon = 10^{-6}$ m, length of the channel $L = 50$ m with frictionless bottom and 500 rectangular meshes.

Fig. 7 to Fig. 10 illustrate the simulation results of these four Riemann problems compared to corresponding analytical solutions. It can be seen our scheme gives perfect agreement with the exact results. It is also observed that test 4 does not capture the dry middle state at time $t = 1.0$ s. The reason could be attributed to the Riemann solver (HLLC) underestimating the front propagation speed. The L^2 error norms for all tests can be found in Table 3.

5.3 Dam-break flooding over three humps

In this test case, the performance of the presented scheme as to deal with complicated wetting/drying process and mass conservation is validated. The problem, which was proposed by Kawahara and Umetsu (1986) and has been widely reconsidered by other researchers (e.g. Song et al., 2011; Liang and Borthwick, 2009), considers a dam-break wave propagation over an initially dry flood plain with three humps. In a channel 75 m long and 30 m wide (triangulated with 5086 elements) the dam is situated at $x = 16$ m with initial water depth $\eta = 1.875$ m, while the

rest of the channel is considered dry. Three humps are located in the channel bottom. The initial condition and the channel geometry can be seen in Fig. 11 on top left. The Manning coefficient $n = 0.018$ for this problem. Solid slip conditions are applied at the lateral walls of the channel.

Numerical results are presented in Fig. 11 for the water movement at different times to show the propagation of the flood. The small humps are covered by the water in its propagation and the effect of advancing and recession over the sloppy bed is clear. The tip of the higher hump is always dry and the accumulation of water can be clearly observed. The collision of the advancing front first with the higher hump and then with the downstream boundary wall can be seen with the expected physical behavior. The generation of dry bed can also be observed for the small humps as time evolves until it reaches a steady state. Fig. 12 illustrates this steady state at $t = 300$ s along with the evolution of the relative mass error with and without mass correction, proving the scheme to be highly conservative.

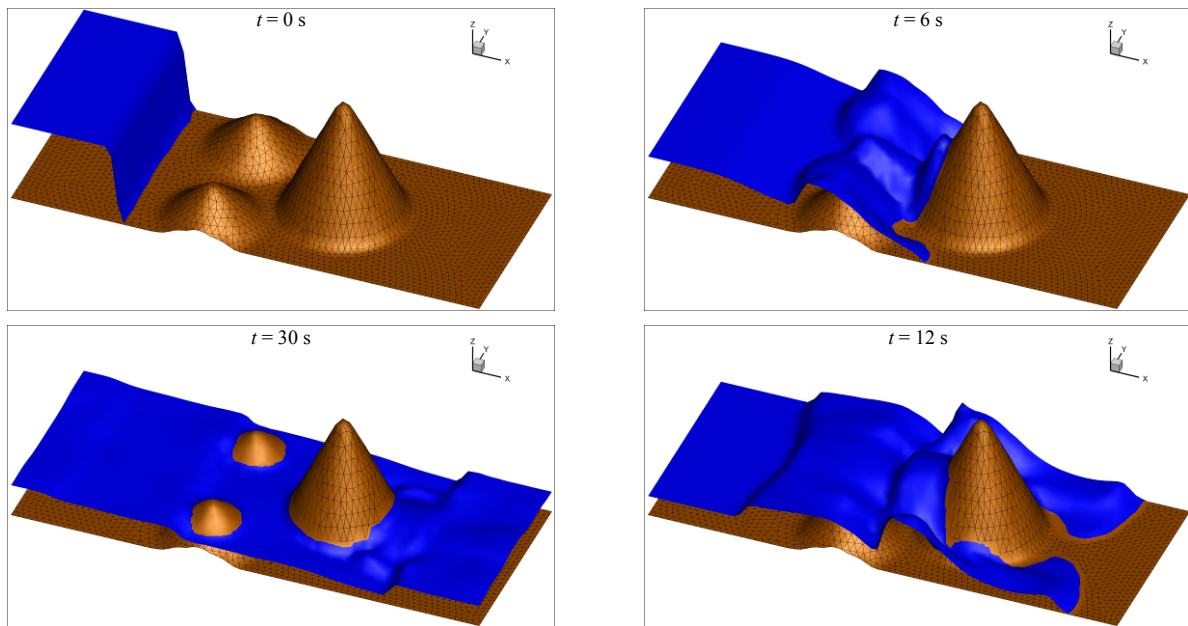


Fig. 11 Dam-break flooding over three humps: depth evolution.

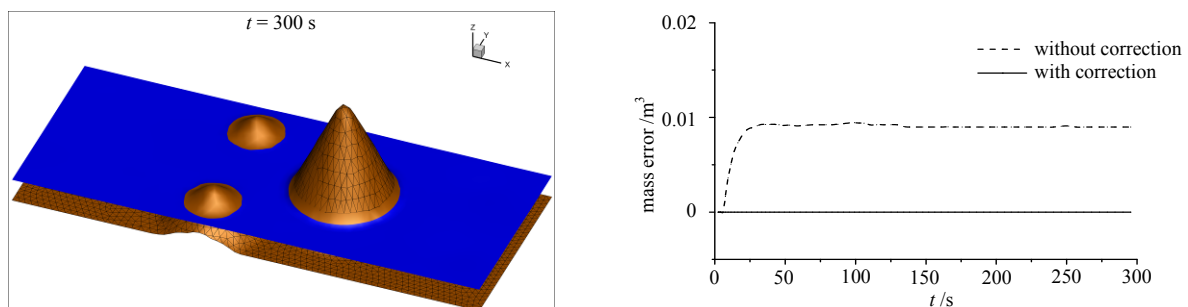


Fig. 12 Dam-break flooding over three humps: final steady state (left) and mass error history (right).

5.4 Tsunami run-up onto a complex 3D beach

The Okushiri tsunami in 1993 produced unexpectedly large run-up heights of up to 31.7 meters at the head of the Monai Valley. The Research Institute for Electric Power Industry (CRIEPI) in Abiko, Japan constructed a 1:400 laboratory model for the area around the island (Liu et al., 2008). All the data we used here can be downloaded from website http://nctr.pmel.noaa.gov/benchmark/Laboratory/Laboratory_MonaiValley/index.html.

The bathymetry and initial tsunami free surface height used in the laboratory and numerical experiments are shown in Fig. 13. Three locations marked by circles in the figure provide the elevation used for the comparison. Note that right, top and bottom boundaries (in the figure plane) are solid walls and the left boundary is open. The numerical mesh covers the area of the experiment

with unstructured hyper cells (8943 quadrangles and 460 triangles, Fig. 13). Due to the convection being dominated in this problem, the viscous effects are neglected. Manning coefficient $n = 0.0025$ and tolerance depth $\varepsilon = 10^{-5}$ m are used here.

The simulated 3D-view surface elevations at various times are shown in Fig. 14. It is observed that after an initial draw-down of the free surface, the tsunami travels onshore with a sudden increased wave height. The diffracted waves by the island meet together behind it at $t = 10\sim 14$ s. Then, around $t = 16\sim 18$ s, the tsunami wave reaches the coast and the reflected waves emerges from the beach. The maximum run-up is up to 7.6 cm at $t = 16.6$ s, which corresponds to 30.4 m at field scale. This is remarkably close to the measured value of 31.7 m. Furthermore in Fig. 15, the computed free surface elevations agree very well at all gauges with experimental results.

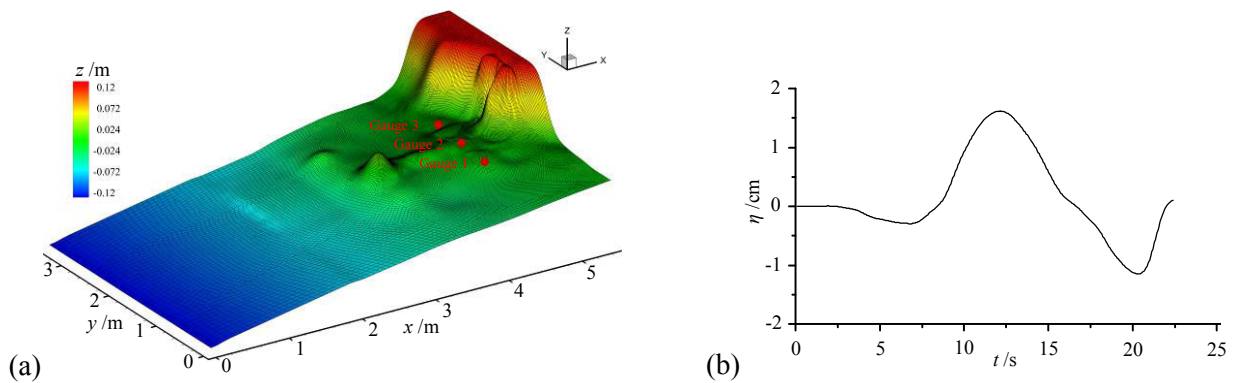


Fig. 13 Tsunami run-up test case: (a) Bathymetry, mesh and three gauge stations; and (b) Input wave.

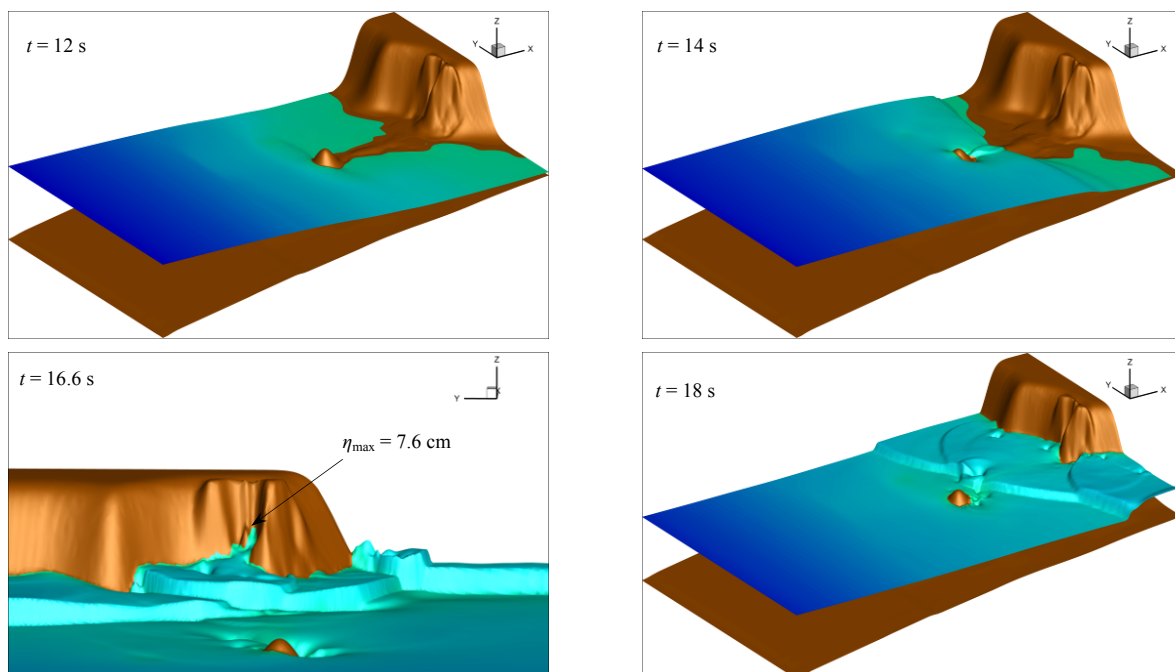


Fig. 14 Tsunami run-up onto complex 3D beach: 3D view at times $t = 12, 14, 16.6$ and 18 s.

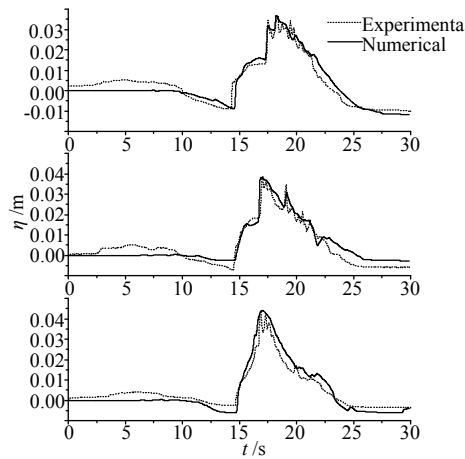


Fig. 15 Comparison of experimental data with numerical simulation at three fixed gauges.

5.5 Malpasset dam-break simulation

The Malpasset dam was located in a narrow gorge of the Reyran river valley in France. It was a 66.5 m high arch dam with a crest length of 223 m and the maximum reservoir capacity of $55 \times 10^6 \text{ m}^3$. In the immediate downstream of the dam, the Reyran river valley is very narrow and has two consecutive sharp bends. Then the valley widens as it goes downstream and eventually reaches the flat plain (see Fig. 16). The dam failed in 1959 following an exceptionally heavy rain. After the dam failure, a field survey was performed to obtain the maximum water levels along the Reyran river valley. In addition, a physical model with a scale of 1/400 was built to study the dam-break flow in 1964. The maximum water level and the flood wave arrival time at 9 points along the river valley were measured (see Fig. 16). Because of its complex topography and availability of measured data, the Malpasset dam-break case was selected as a benchmark test example for dam-break models in the CADAM project (Goutal, 1999). More detailed descriptions about Malpasset dam-break test case can be found

in literature (Goutal, 1999; Hervouet and Petitjean, 1999; Valiani et al., 2002). In the computation, a hybrid unstructured grid has been used, as illustrated in Fig. 16. The initial water level in the reservoir is set to be 100 m above the sea level. The rest of the computational domain is considered as dry bed. A spatially constant value of Manning's coefficient is set equal to 0.033, taken from Valiani et al. (2002). The tolerance depth $\varepsilon = 0.05 \text{ m}$ is considered in the simulation. Along the edges of the model, closed boundary condition is imposed if it is land. In the sea, the free surface water level is just assumed to be constant at 0 m ABS.

The results of the model simulation are compared against historical survey data, physical model data and results from other numerical codes. Fig. 17 gives the process of dam failure. It takes 2280s for the flood to reach the sea after dam-break in the simulation, which is quite close to the recorded time at 2160 s. Table 4 presents the time of flood arriving at three electric transformers compared with measurements. As it shows, good agreement has been achieved. Also, our results are slightly better than those of TELEMAC (Hervouet and Petitjean, 1999) and those from Valiani et al. (2002). The detailed comparisons, concerning the maximum water level reached at the valley sides, among our numerical predictions, TELEMAC's results, Valiani's data and field data are shown in Table 5. Generally, good agreement is achieved. The small differences could be due to several other unquantifiable sources, for instances, the field measurements themselves and topographic data. In Table 6, simulation results at points G6 to G14 are compared with the results reported by Valiani et al. (2002), as well as the results reported by Hervouet and Petitjean (1999). It can be seen that all three numerical models give nearly identical results, which differ far more from the laboratory data than from one another.

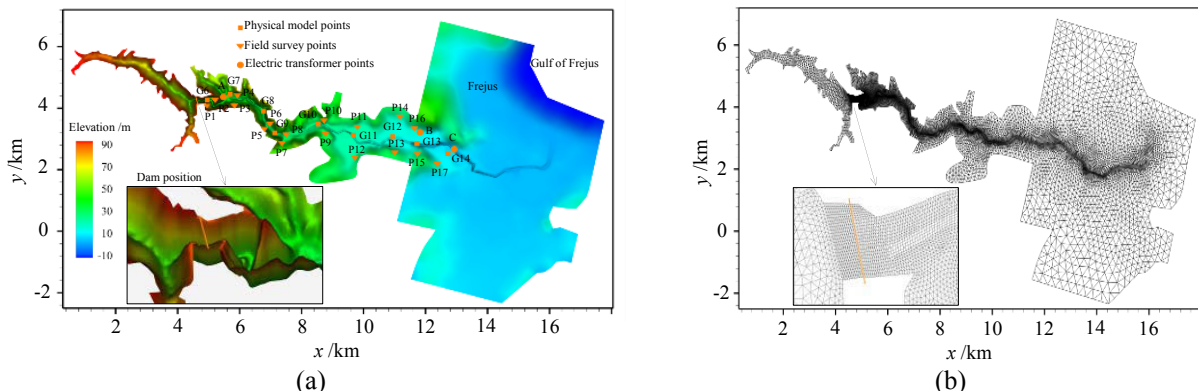


Fig. 16 Malpasset dam: (a) Contour view of topography with locations of field and laboratory points; and (b) Hybrid unstructured grids (2553 quadrangles for riverway and 19412 triangles elsewhere).

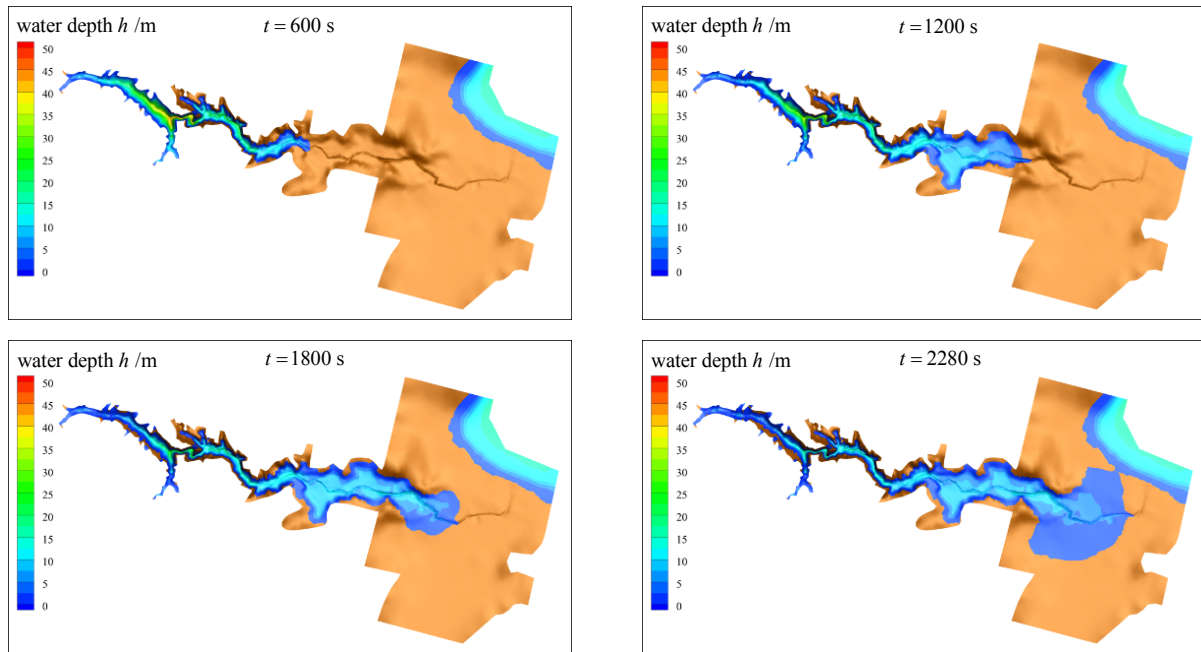
Fig. 17 Malpasset dam-break flow: water depth evolution at times $t = 600, 1200, 1800$ and 2280 s.

Table 4 Comparison of simulated and field electric transformers shutdown time.

Electric transformers	Field data /s	Simulated		Valiani's		Hervouet's	
		t /s	Δ /%	t /s	Δ /%	t /s	Δ /%
A	100	98	-2.0	111	11.0	98	-2.0
B	1240	1265	2.0	1287	3.8	1305	5.2
C	1420	1402	-1.3	1436	1.1	1401	-1.3

Table 5 Points surveyed by police.

Maximum water levels (m)									
Right bank									
Points	P1	P3	P5	P7	P9	P12	P13	P15	P17
Simulated	91.49	52.05	48.39	39.64	32.87	26.01	23.22	18.85	13.89
Valiani's	75.96	53.77	45.56	42.86	32.44	27.35	23.58	19.37	14.23
Field data	79.15	54.90	51.10	44.35	31.90	24.90	17.25	18.60	14.00
Left bank									
Points	P2	P4	P6	P8	P10	P11	P14	P16	
Simulated	91.15	63.70	47.06	36.63	38.93	25.62	20.90	18.63	
Valiani's	89.34	59.64	44.85	34.61	38.12	25.37	23.19	20.39	
Field data	87.20	64.70	43.75	38.60	40.75	24.15	20.70	17.25	

Table 6 Gauges of physical model.

Maximum water levels (m)									
Gauges	G6	G7	G8	G9	G10	G11	G12	G13	G14
Simulated	88.68	54.57	55.42	47.94	37.08	26.26	19.63	18.11	13.22
Valiani's	81.98	53.86	53.80	48.39	36.88	25.54	18.48	17.43	12.60
Hervouet's	87.97	54.43	53.25	47.91	36.51	25.37	19.13	17.65	12.76
Physical model data	84.20	49.10	54.00	40.20	34.90	27.40	21.50	16.10	12.90

6. CONCLUSIONS

A new form of the SWEs, which is mathematically balanced for flux gradients and source terms, is presented on the basis of an unstructured grid and mass conservatized

Godunov-type FVM. The established scheme provides a second order convergence in both space and time using a 4 stages Runge-Kutta method together with linear reconstruction procedure. The present model solves discontinuous solution stably with the

approximate HLLC Riemann solver, handles friction term in semi-implicit scheme and treats wet/dry fronts with zero mass error by the improved approach of Zhao et al. (1994) and a flux correction strategy. All these features enable it to be a much flexible method in solving problems related to complex geometries. Several numerical tests have been performed and the model's accuracy has been validated. The model is also further applied to simulate a realistic flood propagation case. The well-balanced property of the proposed scheme has also been tested by simulating still water over uneven bottom topography. Numerical solution shows a perfect agreement with the analytical solutions in cases of Toro's Riemann problems. The applications of the present model in simulating 2D laboratory tsunami run-ups and the Malpasset dam break event demonstrate that the model is very accurate in solving engineering problems. With the satisfactory performance, this new numerical model hence can be widely used for studying practical shallow water flows.

REFERENCES

1. Alcrudo F, Garcia-Navarro P (1993). A high resolution Godunov-type scheme in finite volumes for the 2D shallow-water equations. *Internal Journal for Numerical Methods in Fluids* 16(6):489-505.
2. Anderson WK, Bonhaus DL (1994). An implicit upwind algorithm for commutating turbulent flows on unstructured grids. *Computers Fluids* 23(1):1-21.
3. Barth TJ, Jespersen DC (1989). The design and application of upwind schemes on unstructured meshes. *AIAA Paper*, 890366.
4. Begnudelli L, Sanders BF (2006). Unstructured grid finite-volume algorithm for shallow-water flow and scalar transport with wetting and drying. *ASCE Journal of Hydraulic Engineering* 132(4):371-384.
5. Bermudez A, Dervieux JA, Vázquez ME (1998). Upwind schemes for the two-dimensional shallow water equations with variable depth using unstructured meshes. *Computer Methods in Applied Mechanics and Engineering* 155:49-72.
6. Bermudez A, Vázquez ME (1994). Upwind methods for hyperbolic conservation laws with source terms. *Computers and Fluids* 23(8):1049-1071.
7. Brufau P, García-Navarro P (2003). Unsteady free surface flow simulation over complex topography with a multidimensional upwind technique. *Journal of Computational Physics* 186(2):503-526.
8. Brufau P, García-Navarro P, Vázquez-Cendón ME (2004). Zero mass error using unsteady wetting-drying conditions in shallow flows over dry irregular topography. *Internal Journal for Numerical Methods in Fluids* 45:1047-1082.
9. Caleffi V, Valiani A, Zanni A (2003). Finite volume method for simulating extreme flood events in natural channels. *Journal of Hydraulic Research* 2:167-177.
10. Choi H, Liu JG (1998). The reconstruction of upwind fluxes for conservation laws: Its behavior in dynamic and steady state calculations. *Journal of Computational Physics* 144:237-256.
11. Dick E (2009). Introduction to finite volume methods in computational fluid dynamics. *Computational Fluid Dynamics*, Chapter 11, Springer.
12. Fraccarollo L, Toro EF (1995). Experimental and numerical assessment of the shallow water model for two-dimensional dam-break type problems. *Journal of Hydraulic Research* 33:843-864.
13. Garcia-Navarro P, Vázquez ME (2000). On numerical treatment of the source terms in shallow water equations. *Computers and Fluids* 29:951-979.
14. Glaister P (1988). Approximate Riemann solutions of the shallow water equations. *ASCE Journal of Hydraulic Engineering* 26(3):293-306.
15. Godunov S (1959). A difference method for numerical calculation of discontinuous solutions of the equations of hydrodynamics. *Mathematicheskii Sbornik* 47(89):271-306.
16. Goutal N (1999). The Malpasset dam failure—An overview and test case definition. *Proceedings of the 4th CADAM meeting*. Nov. 18-19, Zaragoza, Spain.
17. Hanert E, Le Roux DY, Legat V, Deleersnijder E (2005). An efficient Eulerian finite element method for the shallow water equations. *Ocean Modelling* 10:115-136.
18. Harten A, Lax PD, van Leer B (1983). On upstream differencing and Godunov-type schemes for hyperbolic conservation laws. *SIAM Review* 25(1):35-61.
19. Heniche M, Secretan Y, Boudreau P, Leclerc M (2000). A two-dimensional finite element drying-wetting shallow water model for rivers and estuaries. *Advances in Water Resource* 23:359-372.

20. Hervouet JM, Petitjean A (1999). Malpasset dam break revisited with two-dimensional computations. *Journal of Hydraulic Research* 37(6):777-788.
21. Kawahara M, Umetsu T (1986). Finite element method for moving boundary problems in river flow. *International Journal for Numerical Methods in Fluids* 6(6):365-386.
22. LeVeque RJ (1998). Balancing source terms and flux gradients in high-resolution Godunov methods: The quasi-steady wave-propagation algorithm. *Journal of Computational Physics* 146(1):346-365.
23. LeVeque RJ (2002). *Finite Volume Methods for Hyperbolic Problems*. Cambridge University Press.
24. Li W, Ren Y, Lei G, Luo H (2011). The multi-dimensional limiters for solving hyperbolic conservation laws on unstructured grids. *Journal of Computational Physics* 230(21):7775-7795.
25. Liang Q, Borthwick AGL (2009). Adaptive quadtree simulation of shallow flows with wet-dry fronts over complex topography. *Computers and Fluids* 38:221-234.
26. Liu PLF, Yeh H, Synolakis C (2008). *Advanced Numerical Models for Simulating Tsunami Waves and Runup*. World Scientific.
27. Loukili Y, Soulaïmani A (2007). Numerical tracking of shallow water waves by the unstructured finite volume WAF approximation. *International Journal for Computational Methods in Engineering Science and Mechanics* 8(1):1-14.
28. Mohanraj R, Neumeier Y, Zinn B (1999). Characteristic-based treatment of source terms in Euler equations for Roe scheme. *AIAA Journal* 37(4):417-424.
29. Navon IM (1979). Finite-element simulation of the shallow-water equations model on a limited-area domain. *Applied Mathematical Modelling* 3:337-348.
30. Nujic M (1995). Efficient implementation of non-oscillatory schemes for the computation of free-surface flows. *Journal of Hydraulic Research* 33(1):101-111.
31. Osher S, Solomon F (1982). Upwind difference schemes for hyperbolic conservation laws. *Mathematic of Computation* 38(158):339-374.
32. Roe PL (1981). Approximate Riemann solvers, parameter vectors, and difference schemes. *Journal of Computational Physics* 43(2):357-372.
33. Rogers BD, Borthwick AGL, Taylor PH (2003). Mathematical balancing of flux gradient and source terms prior to using Roe's approximate Riemann solver. *Journal of Computational Physics* 192(2):422-451.
34. Sleight PA, Gaskell PH, Berzins M, Wright NG (1998). An unstructured finite-volume algorithm for predicting flow in rivers and estuaries. *Computers and Fluids* 27(4):479-508.
35. Song L, Zhou J, Li Q, Yang X, Zhang Y (2011). An unstructured finite volume model for dam-break floods with wet/dry fronts over complex topography. *International Journal for Numerical Methods in Fluids* 67(8):960-980.
36. Steger JL, Warming RF (1981). Flux vector splitting of the inviscid gasdynamic equations with application to finite-difference methods. *Journal of Computational Physics* 40:263-293.
37. Toro EF (1997). *Riemann Solvers and Numerical Methods for Fluid Dynamics: A Practical Introduction*. Springer.
38. Toro EF (2001). *Shock-Capturing Methods for Free-Surface Shallow Flows*. Wiley, New York.
39. Toro EF, Spruce M, and Spares W (1994). Restoration of the contact surface in the HLL Riemann solver. *Shock Wave* 4:25-34.
40. Valiani A, Caleffi V, Zanni A (2002). Case Study: Malpasset dam-break simulation using a two-dimensional finite volume method. *ASCE Journal of Hydraulic Engineering* 128(5):460-472.
41. Vázquez ME (1999). Improved treatment of source terms in upwind schemes for the shallow water equations in channels with irregular geometry. *Journal of Computational Physics* 148:497-526.
42. Younus M, Chaudhry MH (1994). A depth-averaged k- ϵ turbulence model for the computation of free-surface flow. *Journal of Hydraulic Research* 32(3):415-444.
43. Zhao DH, Shen HW, Tabios III GQ, Lai JS, Tan WY (1994). Finite-volume two dimensional unsteady-flow model for river basins. *ASCE Journal of Hydraulic Engineering* 120(7):863-883.
44. Zhou JG, Causon DM, Mingham CG, Ingram DM (2001). The surface gradient method for the treatment of source terms in the shallow-water equations. *Journal of Computational Physics* 168:1-25.
45. Zhou JG, Causon DM, Mingham CG, Ingram DM (2004). Numerical prediction of dam-

break flows in general geometries with complex bed topography. *ASCE Journal of Hydraulic Engineering* 130(4):332-340.